

THE MOLECULAR GAS ENVIRONMENT AROUND TWO HERBIG Ae/Be STARS: RESOLVING THE OUTFLOWS OF LkH α 198 AND LkH α 225S

BRENDA C. MATTHEWS,^{1,2} JAMES R. GRAHAM,² MARSHALL D. PERRIN,² AND PAUL KALAS²

Received 2007 June 29; accepted 2007 August 9

ABSTRACT

Observations of outflows associated with pre-main-sequence stars reveal details about morphology, binarity, and evolutionary states of young stellar objects. We present molecular line data from the Berkeley-Illinois-Maryland Association array and Five Colleges Radio Astronomical Observatory toward the regions containing the Herbig Ae/Be stars LkH α 198 and LkH α 225S. Single-dish observations of $^{12}\text{CO } J = 1 - 0$, $^{13}\text{CO } J = 1 - 0$, $\text{N}_2\text{H}^+ J = 1 - 0$, and $\text{CS } J = 2 - 1$ were made over a field of $4.3' \times 4.3'$ for each species. $^{12}\text{CO } J = 1 - 0$ data from FCRAO were combined with high-resolution BIMA array data to achieve a naturally weighted synthesized beam of $6.75'' \times 5.5''$ toward LkH α 198 and $5.7'' \times 3.95''$ toward LkH α 225S, representing resolution improvements of factors of approximately 10 and 5 over existing data. By using uniform weighting, we achieved another factor of 2 improvement. The outflow around LkH α 198 resolves into at least four outflows, none of which are centered on LkH α 198-IR, but even at our resolution we cannot exclude the possibility of an outflow associated with this source. In the LkH α 225S region we find evidence for two outflows associated with LkH α 225S itself, and a third outflow is likely driven by this source. Identification of the driving sources is still resolution limited and is also complicated by the presence of three clouds along the line of sight toward the Cygnus molecular cloud. $^{13}\text{CO } J = 1 - 0$ is present in the environments of both stars along with cold, dense gas as traced by $\text{CS } J = 2 - 1$ and (in LkH α 225S) $\text{N}_2\text{H}^+ J = 1 - 0$. No 2.6 mm continuum is detected in either region in relatively shallow maps compared to existing continuum observations.

Subject headings: ISM: clouds — ISM: individual (LkH α 198, LkH α 225S) — ISM: molecules — stars: formation

1. INTRODUCTION

In addition to evidence for mass infall (accretion), many pre-main-sequence stars also possess prominent outflows and jets. These jets are believed to play a crucial role in removing angular momentum from circumstellar disks, allowing accretion to continue (Stahler & Palla 2004). Outflows can extend many parsecs in length, and can serve as “fossil records” of the accretion process, providing indications of temporal variability of accretion or precession of outflow axes over thousands of years (McGroarty & Ray 2004). Furthermore, outflows inject turbulence into molecular clouds and may regulate overall star formation efficiency (Matzner & McKee 2000; McKee & Ostriker 2007).

Outflows from young stars may be observed both through shock-excited emission lines such as [S II] $\lambda\lambda 6716, 6731$ (e.g., Finkenzeller 1985; Corcoran & Ray 1998) and [Fe II] 1.257, 1.644 μm (Graham et al. 1987; Pyo et al. 2003), and also through millimeter rotational lines of CO and other molecules (e.g., Schmid-Burgk et al. 1990; Arce & Sargent 2006). Because star formation is a complex and turbulent process, high angular resolution observations (i.e., submillimeter or millimeter interferometry) are usually required in order to disentangle the various motions of molecular gas around young stars (infall, outflow, rotation, or turbulence). Such observations have been used to probe the kinematics of outflows from a wide range of young stellar objects, including T Tauri stars such as HH 30 (Pety et al. 2006) and deeply embedded Class I protostars such as those in

AFGL 5142 (Zhang et al. 2007), which is a protocluster displaying at least three molecular outflows originating from at least half a dozen embedded massive protostars.

In this paper we consider molecular outflows in an intermediate case between these two extremes, by investigating outflows originating from groups of Herbig Ae/Be (HAeBe) stars. The HAeBe stars are pre-main-sequence stars of intermediate mass, i.e., $1.5 \leq M/M_{\odot} \leq 10$ (Herbig 1960; Waters & Waelkens 1998), which exhibit infrared and millimeter excesses indicative of circumstellar dust. While the majority of outflows studied to date originate from T Tauri stars, many HAeBe stars are known to launch outflows as well (Mundt & Ray 1994), in some cases extending several parsecs in length (McGroarty et al. 2004). HAeBe stars are often found in groups (Testi et al. 1998, 1997), making high angular resolution observations critical for resolving the outflows associated with individual stars. These intermediate-mass stars are also rarer than later type T Tauri stars due to the steepness of the initial mass function, which means they are, on average, found at greater distances than their lower mass counterparts. Therefore, higher angular resolutions are required to resolve their outflows compared to closer, lower mass T Tauri stars.

We have searched for wide-field and high-resolution emission from $^{12}\text{CO } J = 1 - 0$ in the environments around the HAeBe stars LkH α 198-IR and LkH α 225S based on intriguing results from near-IR AO imaging polarimetry by Perrin et al. (2004a). In addition, we have obtained single-dish spectra of $^{13}\text{CO } J = 1 - 0$, $\text{CS } J = 2 - 1$, and $\text{N}_2\text{H}^+ J = 1 - 0$ toward both sources. We present here millimeter observations of the LkH α 198 and LkH α 225S stars and their nearby group members. Our high angular resolution observations resolve multiple outflows in both of these regions. The observations and data reduction techniques are described in § 2. Results for LkH α 198 and LkH α 225S and their surrounding

¹ Herzberg Institute of Astrophysics, National Research Council of Canada, 5071 West Saanich Road, Victoria, BC, V9E 2E7 Canada; brenda.matthews@nrc-nrc.gc.ca.

² Department of Astronomy, University of California, Berkeley, CA 94720-3411.

TABLE 1
FCRAO OBSERVATIONAL SUMMARY

Source	Species/Transition	Frequency (GHz)	Antenna Efficiency	Resolution (km s ⁻¹)	Sensitivity per Channel (K)
LkH α 198.....	¹² CO $J = 1 - 0$	115.21720	0.45	0.06349	0.35
	¹³ CO $J = 1 - 0$	110.20135	0.49	0.06642	0.15
	N ₂ H ⁺ $J = 1 - 0$	93.17378	0.52	0.07855	0.09
	CS $J = 2 - 1$	97.98095	0.52	0.07470	0.09
LkH α 225S.....	¹² CO $J = 1 - 0$	115.21720	0.45	0.06350	0.40
	¹³ CO $J = 1 - 0$	110.20135	0.49	0.06642	0.16
	N ₂ H ⁺ $J = 1 - 0$	93.17378	0.52	0.07470	0.09
	CS $J = 2 - 1$	97.98095	0.52	0.07856	0.09

regions are presented in §§ 3 and 4, respectively. Our findings are summarized in § 5.

2. OBSERVATIONS AND DATA REDUCTION

2.1. FCRAO Data

We obtained ¹²CO $J = 1 - 0$, ¹³CO $J = 1 - 0$, CS $J = 2 - 1$, and N₂H⁺ $J = 1 - 0$ data from the 14 m Five Colleges Radio Astronomical Observatory (FCRAO) using the array SEQUOIA on 2004 November 10. The telescope was pointed toward LkH α 198 at $\alpha_{J2000.0} = 00^{\text{h}}11^{\text{m}}25.97^{\text{s}}$, $\delta_{J2000.0} = +59^{\circ}49'29.1''$ and LkH α 225S at $\alpha_{J2000.0} = 20^{\text{h}}20^{\text{m}}30.65^{\text{s}}$, $\delta_{J2000.0} = +41^{\circ}21'25.50''$. A fully sampled image covering a field of view $4.3' \times 4.3'$ was made of four spectral line transitions. The transitions ¹²CO $J = 1 - 0$ and ¹³CO $J = 1 - 0$ were observed simultaneously; similarly, CS $J = 2 - 1$ and N₂H⁺ $J = 1 - 0$ were obtained in a single observation. A summary of the FCRAO observations is shown in Table 1. Each observation was 24 minutes in duration. Calibrated T_A^* data are delivered from the telescope. We converted these data to main-beam temperatures by division of the appropriate antenna efficiency (see Table 1). The conversion to Jy beam⁻¹ was done by deriving the conversion factor based on the observing wavelength and telescope beam:

$$\frac{\text{Jy}}{\text{K}} = \left[13.6 \frac{\lambda(\text{mm})^2}{\theta''_{\min} \theta''_{\max}} \right]^{-1}, \quad (1)$$

where θ''_{\min} and θ''_{\max} are the minor and major axes of the telescope beam. For single-dish millimeter telescopes, the axes are equal and equivalent to the diffraction limit of the antenna. For FCRAO, the conversion factor is 23.6 Jy K⁻¹. The beam size (resolution) is 46.7'' for ¹²CO $J = 1 - 0$, 48.9'' for ¹³CO $J = 1 - 0$, 55.0'' for CS $J = 2 - 1$, and 57.5'' for N₂H⁺ $J = 1 - 0$.

The data were taken in the 25 MHz mode. The rms sensitivity per channel is shown in Table 1 for each transition.

2.2. BIMA Interferometric Data

We observed the regions surrounding the two HAeBe multiple systems in single pointings with the Berkeley-Illinois-Maryland Association (BIMA) interferometer³ (Welch et al. 1996) in Hat Creek, CA. The data were taken on 2003 October (1 track each), followed by multiple observations over the period from 2004 March to 2004 June (see Table 2). For both regions, we used the same target coordinates as for the FCRAO observations.

Three configurations of the 10 6.1 m antennas were used to observe the ¹²CO $J = 1 - 0$ line and continuum at 2.7 mm. An A-array track and a D-array track toward LkH α 225 were not used due to poor phase correlations. Two B-array tracks toward LkH α 198 were rejected for the same reason. The D-array, C-array, and B-array data have projected baselines between 2 and 13 k λ , 2 and 33 k λ , and 3 and 74 k λ , respectively. Table 2 contains the sensitivities achieved per usable track.

The ¹²CO $J = 1 - 0$ line was observed utilizing the digital correlator to record the line in four bands, configured in redundant bandwidths of 12.5 MHz (256 channels) and 50 MHz (128 channels), giving spectral resolutions of 0.127 and 1.016 km s⁻¹ for LkH α 198. The same configuration was used for the C-array track of LkH α 225S. For the 2004 tracks toward LkH α 225S, we allocated 256 channels each across bandwidths of 12.5 and 25 MHz, resulting in velocity resolutions of 0.127 and 0.254 km s⁻¹, respectively. LkH α 198 was also observed in some LkH α 225S tracks, when the latter source was too high in elevation to be observed. The lower sideband was used to measure the continuum

³ The BIMA Array was operated by the Berkeley-Illinois-Maryland Association under funding from the National Science Foundation.

TABLE 2
SUMMARY OF ¹²CO $J = 1 - 0$ OBSERVATIONS AT 115.21720 GHz

Source	Date	Array Configuration	Resolution (km s ⁻¹)	Sensitivity per Channel (Jy beam ⁻¹)
LkH α 198.....	2004 Mar 1	B	0.127	4.6
	2004 Mar 4	B	0.127	5.7
	2004 Mar 18	B	0.127	6.6
	2004 Mar 29	B	0.127	3.4
	2004 Apr 26	C	0.127	1.9
	2004 Jun 1	D	0.127	1.8
LkH α 225S.....	2003 Oct 28	C	0.127	2.7
	2004 Mar 4	B	0.254	0.85
	2004 Mar 21	B	0.254	1.6
	2004 May 31	D	0.127	5.9

TABLE 3
FINAL PARAMETERS OF COMBINED FCRAO+BIMA $^{12}\text{CO } J = 1-0$ MAPS

Source	Channel Width (km s^{-1})	Final Beam	Weighting	rms per Channel (Jy beam^{-1})
LkH α 198.....	0.127	$6.75'' \times 5.47''$ at -87°	Natural	0.66
	0.127	$3.39'' \times 2.37''$ at -82.5°	Uniform	1.4
LkH α 225S.....	0.254	$5.67'' \times 3.95''$ at -79°	Natural	0.45
	0.254	$2.87'' \times 2.29''$ at -89°	Uniform	0.70

emission at 2.6 mm in bandwidths (125 and 75 MHz for the respective configurations) limited by the spectral line correlator configuration. The typical BIMA array continuum bandwidth was 800 MHz.

Phase and amplitude variations were calibrated by observing quasars at small angular separations from the source fields: 2015+372 and 0102+584 (for LkH α 225S and LkH α 198, respectively) approximately every 30 minutes. The adopted fluxes of these quasars were epoch dependent and measured against observations of the planet Uranus or the quasar 3C 454.3 when possible. The calibration was performed using the MIRIAD (Multichannel Image Reconstruction, Image Analysis and Display; Sault et al. 1995) task MSELFAL. Absolute flux calibration was done using Uranus when observed or by using the derived fluxes of gain calibrators during the same epoch as our observations (utilizing the catalog of fluxes at “plot_swflux” on the BIMA Web site⁴).

Subsequent processing of the data, including the combination of data from different configurations, was done with MIRIAD. Images were produced using MIRIAD’s INVERT algorithm with natural weighting and then by variation of the “robust” parameter to produce a uniform-weighted images optimized for both signal to noise and spatial resolution. The images were then deconvolved using CLEAN and then convolved with the clean beam using RESTOR. The resulting resolutions and sensitivities of the BIMA data are shown in Table 2. The resulting noise levels in naturally weighted images are 0.9 Jy beam^{-1} in 0.127 km s^{-1} channels for the $^{12}\text{CO } J = 1 - 0$ line emission from LkH α 198 and $0.75 \text{ Jy beam}^{-1}$ in 0.254 km s^{-1} channels for LkH α 225S. The rms levels in the continuum maps are 18.5 and $17.0 \text{ mJy beam}^{-1}$ toward LkH α 198 and LkH α 225S, respectively. We achieved naturally weighted FWHM spatial resolutions of $7.4'' \times 6.0''$ and $5.5'' \times 4.1''$ for the continuum maps of the two fields.

2.3. Combination of FCRAO and BIMA Data

The $^{12}\text{CO } J = 1 - 0$ data from FCRAO and the BIMA array were combined to produce total power data cubes. The $^{12}\text{CO } J = 1 - 0$ emission is strongly detected toward both sources, so we have used the highest possible spectral resolution data for combination with the FCRAO data. In the observation of LkH α 225S, one spectral window exhibited evidence of corrupt spectra; therefore, we utilized a redundant observation in a second spectral window for that source. The FCRAO data were reordered to match the BIMA axes (x, y, v) and rescaled to janskys. The MIRIAD task REGRID was then used to interpolate the FCRAO data onto the BIMA data cube. We used the linear combination algorithm of Stanimirovic et al. (1999) to combine the naturally weighted BIMA array dirty map with the single-dish map, using the ratio of the beams as the weighting factor. The combined image was then deconvolved and convolved with the clean beam to reconstruct the total $^{12}\text{CO } J = 1 - 0$ emission.

Maps were created with natural and uniform weighting. The resultant resolutions and sensitivities are summarized in Table 3. The primary beam of the BIMA array antennas at 115 GHz is $1.8'$, which is the area of the resultant combined data maps.

3. LkH α 198 AND ENVIRONS

LkH α 198 (V* V633 Cas, IRAS 00087+5833) is an HAeBe star located at ~ 600 pc based on the interstellar extinction law (Racine 1968; Chavarría-K. 1985). Hillenbrand et al. (1992) categorize LkH α 198 as an A5 pre-main-sequence star, while Hernández et al. (2004) find a spectral type of $B9 \pm 2.5$. LkH α 198 is classified as a Group II HAeBe star in the nomenclature of Hillenbrand et al. (1992), meaning that the spectral energy distribution rises with wavelength in the infrared. Group II HAeBe stars have significant circumstellar envelopes that reprocess stellar radiation at long wavelengths. A strong CO bipolar outflow is associated with this region, but it is not centered on LkH α 198, but rather to the northwest (Cantó et al. 1984; Bally & Lada 1983). Strom et al. (1986) detected evidence of a blueshifted optical flow extending to the east-southeast of LkH α 198, which did not coincide with the redshifted CO emission in that direction. An infrared companion (LkH α 198-IR) was identified approximately $6''$ north of LkH α 198 by Lagage et al. (1993). A submillimeter source (LkH α 198 mm) was identified $19''$ northwest of LkH α 198 at $800 \mu\text{m}$ by Sandell & Weintraub (1994), who also found evidence for CO outflows in the three sources LkH α 198, LkH α 198 mm, and V376 Cas. This source is another HAeBe star in the region, located about $40''$ north of LkH α 198. LkH α 198 mm was also strongly detected in a 1.3 mm observation of the region by Henning et al. (1998). Hajjar & Bastien (2000) classify this source as an extreme Class I object. High-resolution interferometry toward LkH α 198 and the surrounding region at 2.7 mm failed to detect LkH α 198, but LkH α 198 mm was detected and resolved (Di Francesco et al. 1997). High-resolution laser guide star adaptive optics imaging polarimetry by Perrin et al. (2004a) revealed a centrosymmetric polarimetric pattern consistent with a conical cavity. They also detected a “cometary” structure in *JHK* intensity images. Their data suggest that this structure is associated with LkH α 198-IR.

3.1. Observational Results

3.1.1. Moment and Channel Maps

Figure 1 shows the zeroth moment of the combined map of $^{12}\text{CO } J = 1 - 0$ emission toward the LkH α 198 region from the combination of channels from -4 to 4 km s^{-1} and the distribution of emission at velocities blueward and redward of the systemic local standard of rest (LSR) source velocity, -0.7 km s^{-1} (Cantó et al. 1984). The moment maps were created by using only channels with flux densities exceeding 1 Jy beam^{-1} , approximately 1.5 times the rms level per channel. The velocity ranges over which they are taken are specified in Figure 1. The resolution in this map is an order of magnitude improved over the $^{12}\text{CO } J = 1 - 0$ maps of Cantó et al. (1984), but covers an area limited

⁴ See <http://bima.astro.umd.edu>.

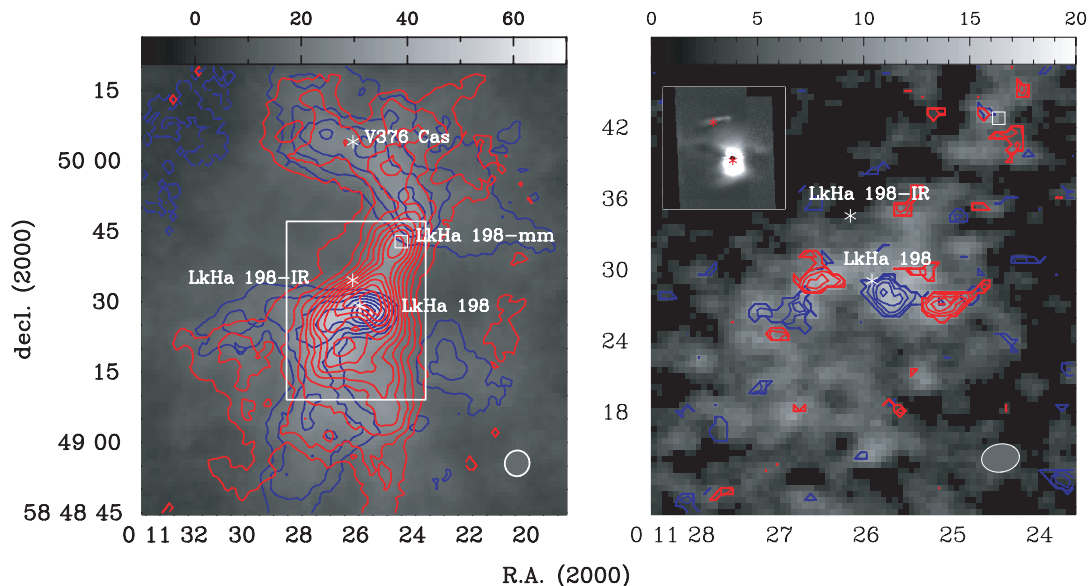


FIG. 1.—*Left*: Gray scale showing the zeroth moment over the entire range of CO emission (-4 to 4 km s^{-1}) of the combined FCRAO+BIMA data toward the region surrounding LkHa 198 (in units of Jy beam $^{-1}$ km s^{-1}). Optically visible HAeBe stars are marked as stars, while the embedded millimeter source is indicated by the square. Contours illustrate the emission to the blue (-4 to -1 km s^{-1}) and to the red (1 to 4 km s^{-1}) of the peak. The contour levels range from 5.2 to 26 Jy beam $^{-1}$ km s^{-1} in steps of 2.6 Jy beam $^{-1}$ km s^{-1} . The resolution is $6.75'' \times 5.5''$. At 600 pc, the beam corresponds to a linear scale of 4000×3300 AU. The box indicates the field of view of the uniformly weighted image at right. *Right*: High-resolution data cube produced from uniformly weighted BIMA array data combined with FCRAO data. The gray scale shows zeroth moment over the entire range of CO emission (-4.0 to 4.2 km s^{-1}). The blue and red contours show the zeroth moments over the ranges from -4.0 to -2.1 km s^{-1} and 2.3 to 4.2 km s^{-1} , respectively. The contour levels range from 1.8 to 4.2 Jy beam $^{-1}$ km s^{-1} in steps of 0.6 Jy beam $^{-1}$ km s^{-1} . The resolution of $3.4'' \times 2.4''$ (2040 AU \times 1440 AU) highlights primarily small features in the outflowing gas. This map shows that no significant red- or blueshifted emission is associated with the LkHa 198-IR source. For comparison, the polarized intensity in H band as measured by Perrin et al. (2004a) is shown in the inset. The LkHa 198 and LkHa 198-IR sources are marked on this image.

by the primary beam of the BIMA array antennas. Strong ^{12}CO $J = 1 - 0$ emission is concentrated around LkHa 198 rather than LkHa 198-IR to the north. We have not detected any structures similar to the dust extension from LkHa 198-IR observed in near-IR polarimetry data (Perrin et al. 2004a).

The second panel of Figure 1 shows a higher resolution image of the region surrounding LkHa 198 and LkHa 198-IR produced by uniformly weighting the BIMA array data before combination with the FCRAO map. The CO features in this map are concentrated around LkHa 198, with no significant emission detected around LkHa 198-IR. Blue- and redshifted emission peaks are paired on either side of LkHa 198. If these each represent individual outflows driven by independent sources, then the driving sources are not evident, as no sources of strong dust emission are located at the central positions between the red and blue peaks. Instead, it is more likely that the peaks represent parts of an outflow from LkHa 198 which may be precessing over time. Such precession can occur when the outflow's driving source is a member of a multiple system. Smith et al. (2005) show that LkHa 198 is a spectroscopic binary with a separation of 60 mas.

Figure 2 shows binned channel maps with 1 km s^{-1} steps around the $V(\text{LSR})$ velocity of -0.7 km s^{-1} . In the blueshifted channels, the dominant feature is the arc of emission that traces out the edges of the southeast elliptical cavity detected in the I-band image of Lagage et al. (1993) and the J-band image of Koresko et al. (1997). This feature appears more strongly focussed on LkHa 198 than the adjacent LkHa 198-IR. A secondary blueshifted feature to the north (extending off the map area) may be a component of the outflow originating at LkHa 198 mm. The channels around the cloud's velocity are strongly dominated by cloud emission, but the peak associated with LkHa 198 persists over most channels. By the 1.2 km s^{-1} channel, a redshifted outflow component can be associated with LkHa 198 mm.

The redshifted counterpart to the LkHa 198 outflow appears along the same axis. At the highest velocity shown, 3.3 km s^{-1} , components of the two outflows can be distinguished. Interestingly, redshifted emission to the south and southeast also seems to trace out the elliptical cavity detected by Lagage et al. (1993) in the optical. Interestingly, we find no strong ^{12}CO $J = 1 - 0$ features associated with LkHa 198-IR.

We note that Figure 1 may seem initially at odds with the results of Figure 3 of Cantó et al. (1984), who report single-dish detection of ^{12}CO $J = 1 - 0$ in a $66''$ beam. The red-lobe peak was found to extend to the southeast and to be centered on LkHa 198, with a $1.5'$ offset to the blue peak to the northwest. Cantó et al. (1984) did note that their observations did not depict lobes symmetric about the star, as is more typical for a bipolar outflow, but they did interpret the blue- and redshifted emission as an outflow driven by LkHa 198. It is noteworthy as well that blueshifted optical emission was detected to the southeast of LkHa 198 by Strom et al. (1986). Our single-dish FCRAO data have higher angular resolution ($46.7''$) than the Cantó et al. (1984) map. We have therefore convolved our FCRAO data to $66''$ resolution (see Fig. 3). When compared to the existing data set, we find a similar morphology in the zeroth moment map, with a single prominent red lobe to the southeast and a blue lobe to the northwest. The FCRAO plot in Figure 3 has been generated using the same range in velocity as Figure 3 of Cantó et al. and plotted with comparable flux density levels. At a resolution of $66''$, the emission in the region is strongly dominated by redshifted emission which is centered on the LkHa 198/198-IR sources. The blueshifted emission in the map lies approximately $1'$ to the north (as found by Cantó et al. 1984). The fact that the outflow has been acknowledged to be very asymmetric about the attributed driving source, either LkHa 198 or LkHa 198-IR (Cantó et al. 1984; Nakano et al. 1990), could point to multiple driving sources, but could also

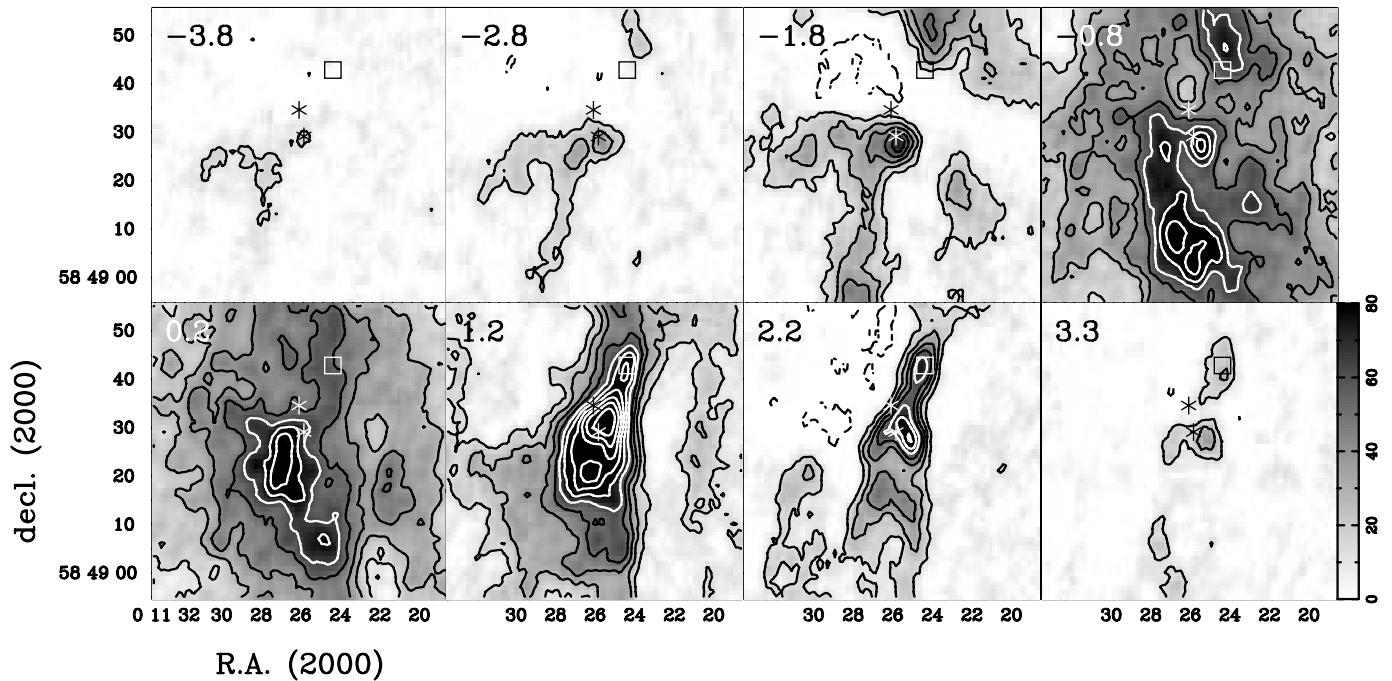


FIG. 2.— Binned intensity images of $^{12}\text{CO } J=1-0$ from combined FCRAO and BIMA array data toward the LkH α 198 region is shown in gray scale and contours over 1.016 km s^{-1} bins. The mean velocity per channel is noted. The gray-scale range is common to all channels and is shown at right (Jy beam^{-1}). The contours are plotted at $20-200 \sigma$ in steps of 20σ , where $\sigma = 0.64 \text{ Jy beam}^{-1}$ is the rms level in a single channel before binning. Sources are marked by asterisks and the square as in Fig. 1.

be explained if the outflow is not much inclined from the line of sight.

The ambiguity regarding the asymmetric nature of the outflow is resolved by the zeroth moments of the BIMA array data alone, which are also shown in Figure 3. This map sharply illustrates the effect of a tenfold improvement in resolution on the interpretation of the number and orientation of outflows in a region containing multiple sources. Even though we are only sensitive to structures on limited spatial scales with these data, the features in red and blue emission can be more clearly associated with individual objects than is possible based on single-dish observations. Figure 3 shows that the red lobe resolves into distinct features, likely associated with LkH α 198 and/or LkH α 198-IR, a distinct red peak associated with LkH α 198 mm, and larger scale blue- and redshifted emission in the vicinity of V376 Cas. Whether the blue-shifted emission to the southeast is driven by LkH α 198 or LkH α 198-IR cannot be easily distinguished in this map, since their small separation of $5''$ is comparable to our resolution. However, the channel maps of Figure 2 do favor LkH α 198 as the driving source for both outflows originating in that small area. The improved resolution of our data explains the coincidence of the blueshifted optical flow defined by the $[\text{S II}]$ emission of Strom et al. (1986) within the redshifted CO outflow lobe detected by Cantó et al. (1984).

With the higher resolution data in hand, we can interpret the single-dish data as follows. The redshifted emission originating from the LkH α 198/198-IR objects completely dominates the emission near the four sources, with the weaker blue lobe shifted north because it originates from one or both of V376 Cas or LkH α 198 mm. This general $^{12}\text{CO } J=1-0$ morphology in Figure 1 is discernible from the $\text{CO } J=2-1$ emission of Sandell & Weintraub (1994) observed with $20''$ resolution with the James Clerk Maxwell Telescope, which shows that blueshifted and redshifted emission overlap southeast of the LkH α 198/198-IR sources and that secondary blue and redshifted peaks are seen $>1'$

north of these objects. However, with the superior resolution of the BIMA array (and the removal of large-scale emission from the maps), the outflow structure can be resolved.

3.1.2. Spectra

In addition to the images presented above, we can construct spectra toward the known point sources in the field, including LkH α 198. Such spectra can indicate whether line emission is optically thick or self-absorbed (from the line shape) or if high-velocity gas is associated with a given position (through the presence of emission in the line wings).

Figure 4 presents the $^{12}\text{CO } J=1-0$ high spatial and spectral resolution data from the combined FCRAO and BIMA array data cubes toward each of the four sources in the LkH α 198 region. The spectral resolution of 0.127 km s^{-1} is a modest factor of 2 improvement from the work of Cantó et al. (1984). Strong self-absorption is evident toward each of the HAeBe objects of Figure 4, indicating that each remains embedded within the nascent molecular cloud. Line wings are detected toward both LkH α 198 and LkH α 198 mm, while there is a suggestion of some redshifted higher velocity emission toward LkH α 198-IR, although this feature could be associated with the ambient cloud material since it arises in the combined spectra, but is not apparent in BIMA array data alone.

Our FCRAO spectral line data enables us to assess whether tracers of dense $[N(\text{H}_2) \sim 10^5 \text{ cm}^{-3}]$ gas such as $\text{CS } J=2-1$ and $\text{N}_2\text{H}^+ J=1-0$ are present in the environment around LkH α 198. Figure 4 shows $^{12}\text{CO } J=1-0$, $^{13}\text{CO } J=1-0$, and $\text{CS } J=2-1$ emission from FCRAO (integrated from a regridded map to match the BIMA array pixel scale, map size, and velocity resolution). $\text{N}_2\text{H}^+ J=1-0$ was not detected anywhere in the observed field. The $\text{CS } J=2-1$ emission is peaked toward the self-absorption of the spectra derived from the high spatial resolution combined data. This is not surprising, since the $\text{CS } J=2-1$, despite the limited spatial resolution of the maps,

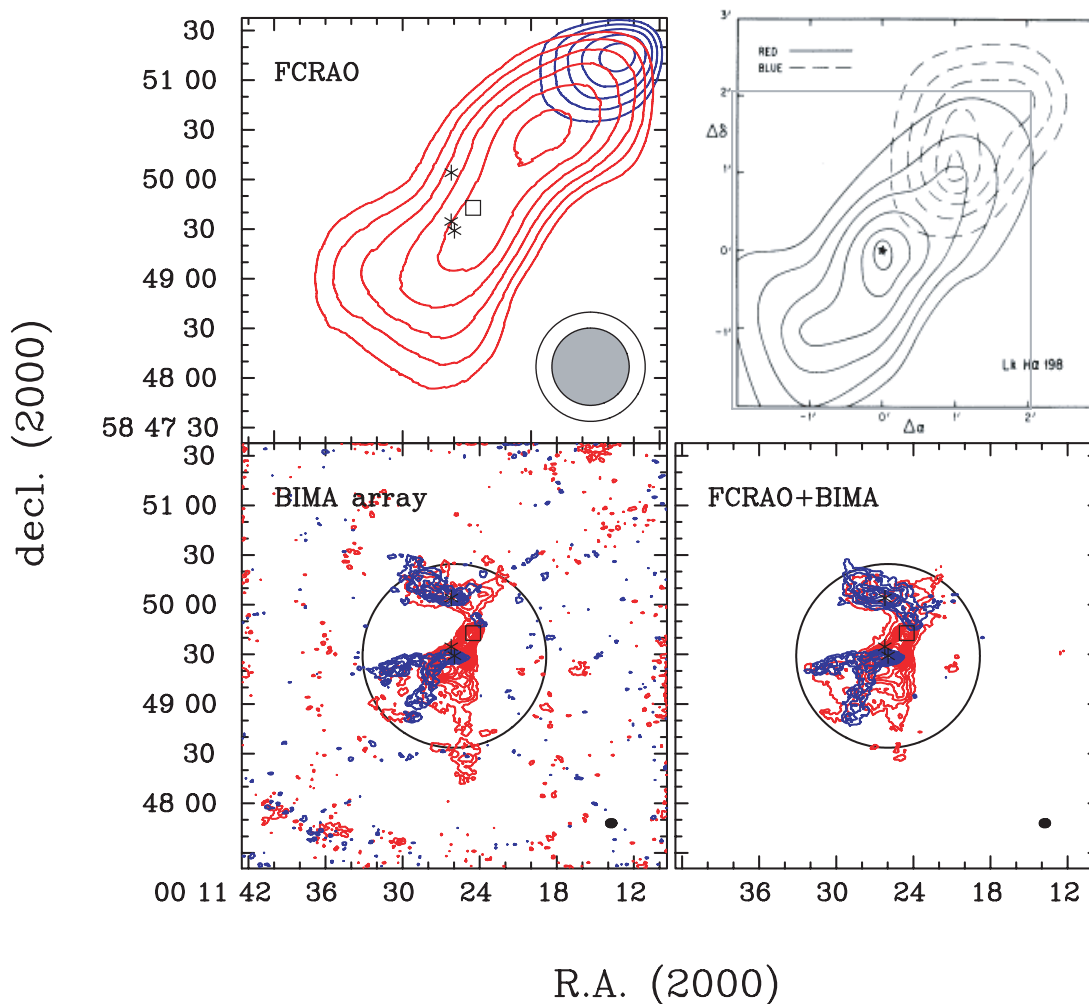


FIG. 3.— Zeroth moment maps of the LkH α 198 region in $^{12}\text{CO } J = 1 - 0$ from FCRAO (*top left*), the BIMA array (*bottom left*) and the combined data set (*bottom right*). Fig. 3 of Cantó et al. (1984) is reproduced at the top right. The gray box shows the area covered by our maps. The contours of the FCRAO image are produced by integration over the same velocity channels as Cantó et al. (i.e., -4.7 to -1.5 km s^{-1} for the blueshifted emission and 0.7 to 3.9 km s^{-1} for the redshifted emission) and plotted at comparable levels (312 to 468 Jy beam^{-1} in steps of 52 Jy beam^{-1}). Channels with flux densities less than 35 Jy beam^{-1} were not included. The elongated red lobe dominates the emission. The blue lobe of Cantó et al. (1984) is just detected at the northwest edge of our map, which is less extensive in that direction. The resolution of the FCRAO data is $46.7''$ (*gray circle*), which we have convolved to $66''$ (*white circle*) to equal the resolution of the Cantó et al. (1984) map. The BIMA array data are integrated over the same velocity ranges, with only channels with flux densities exceeding 1 Jy beam^{-1} included. The circle denotes the primary beam of BIMA at 115 GHz . This is effectively the edge of sensitivity in the BIMA and combined maps. The combined FCRAO+BIMA map is made with the same contour levels as shown in Fig. 1 and is integrated over the same velocities. The BIMA array and combined maps have a synthesized beam of $6.75'' \times 5.5''$ as indicated at the bottom right of those maps. The sources are indicated by asterisks and the square as for Fig. 1.

indicates the presence of relatively high density material ($\sim 10^4 \text{ cm}^{-3}$). For the two northern sources, the CS $J = 2 - 1$ peak also aligns well with the peak of the $^{13}\text{CO } J = 1 - 0$ and the absorption feature of single dish $^{12}\text{CO } J = 1 - 0$, at 0.3 km s^{-1} . For the two southern sources, the $^{13}\text{CO } J = 1 - 0$ peak appears somewhat blueshifted compared to the CS $J = 2 - 1$ peak, with the greatest offset toward LkH α 198.

Ideally, we could use the high spatial resolution to solve for the $V(\text{LSR})$ as a function of position across the region. However, the $^{12}\text{CO } J = 1 - 0$ emission spectra are too complex to be easily fit for single $V(\text{LSR})$ solutions. The CS $J = 2 - 1$ emission would be ideal, but for this species we have only FCRAO data. These data show no significant variation in peak velocity position across the FCRAO maps (i.e., $4'$).

A comparison of the $^{12}\text{CO } J = 1 - 0$ spectra from the single dish alone and the combined map (notably with different beams) indicates that the line wings are much more prominent in the spectra in which the BIMA array data are included. High-resolution

data enable us to discriminate between sources, e.g., clarifying the absence of line wings toward LkH α 198-IR. In addition, these data have increased sensitivity to outflow features which are significantly beam diluted in the single-dish maps. LkH α 198 has extensive line wings shifted blueward and redward of the source's velocity. Toward LkH α 198 mm and V376 Cas, the redshifted emission is more prominent than the blueshifted emission in the combined data, but the opposite appears to be true in the single-dish data, perhaps indicating that the blue lobe of the outflow is more diffuse than its red counterpart. We also note that evidence for a blue wing is apparent in the $^{13}\text{CO } J = 1 - 0$ spectrum toward V376 Cas.

3.1.3. 2.6 mm Continuum

No 2.6 mm continuum emission was detected toward the LkH α 198 region. This is consistent with the absence of a detection at 2.7 mm of dust emission toward LkH α 198 and V376 Cas by Di Francesco et al. (1997). Even in regions of $^{12}\text{CO } J = 1 - 0$ and

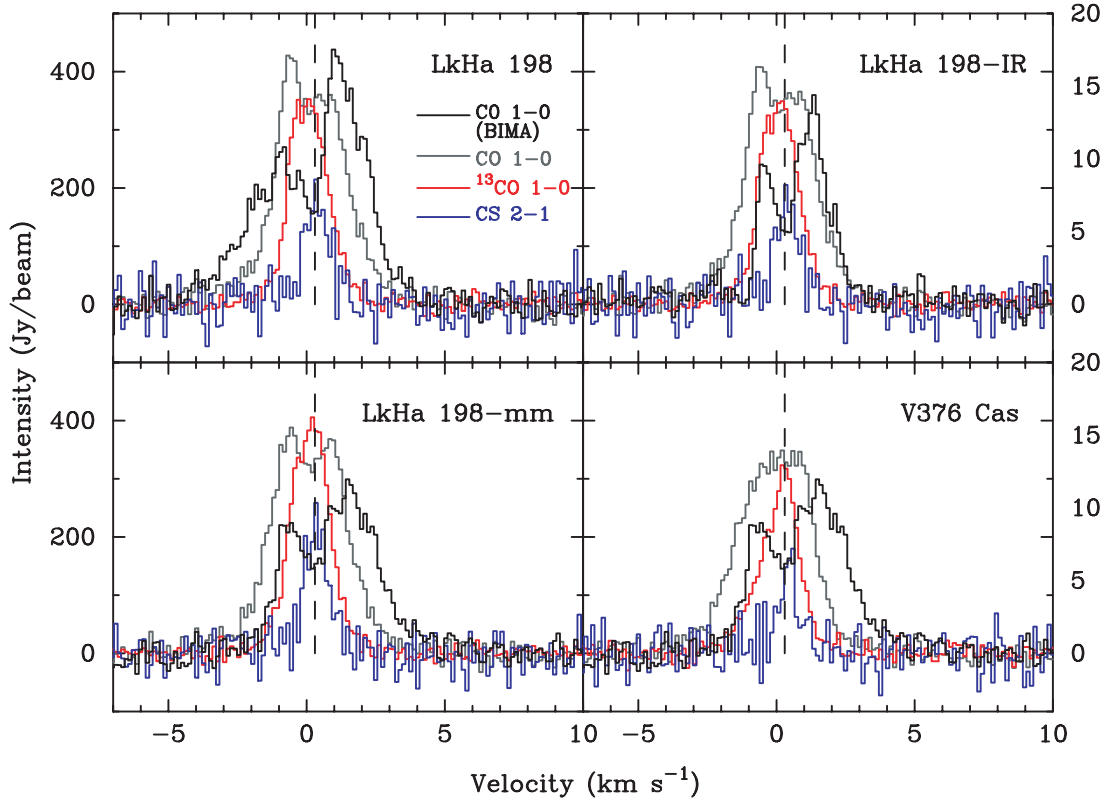


FIG. 4.— Spectra toward individual sources in the LkH α 198 region from FCRAO and FCRAO+BIMA array data. The spectral resolution is 0.127 km s^{-1} . Gray, red, and blue spectra represent $^{12}\text{CO } J=1-0$, $^{13}\text{CO } J=1-0$, and CS $J=2-1$ observations from FCRAO which were regridded to the spatial and spectral scales of the FCRAO+BIMA $^{12}\text{CO } J=1-0$ map. The intensity scale at left is for the single-dish $^{12}\text{CO } J=1-0$ emission. The $^{13}\text{CO } J=1-0$ and CS $J=2-1$ emission have been multiplied by factors of 2 and 20. The black spectra are taken from the combined $^{12}\text{CO } J=1-0$ map. The intensity scale is shown at right. Self-absorption is noted toward each source in the field in both the single dish and combined $^{12}\text{CO } J=1-0$ spectra. The strongest evidence of high-velocity line wings is observed toward LkH α 198 and LkH α 198 mm. Some redshifted emission is observed toward LkH α 198-IR.

$\text{N}_2\text{H}^+ J=1-0$ emission, no continuum emission is evident down to a threshold of 57 mJy beam^{-1} , which is our 3σ limit. Di Francesco et al. (1997) did detect 2.7 mm emission toward LkH α 198 mm using the Plateau de Bure IRAM interferometer. They detected a peak flux density of $S_\nu = 13 \text{ mJy beam}^{-1}$, with a resolution of $9.7'' \times 5.1''$ and an integrated flux density of $24 \pm 6.9 \text{ mJy}$. Our rms level of $18.5 \text{ mJy beam}^{-1}$ is insufficient to detect this flux density. Our lack of detections also indicates that there is no significant free-free emission in the region.

3.2. Individual Objects

We summarize some general findings toward each source in our two fields in Table 4. Some sources are associated with CO emission, but not definitively with an outflow. All four sources in the LkH α 198 field are associated with local $^{12}\text{CO } J=1-0$ emission, as revealed by the strong self-absorption in each of the spec-

tra of Figure 4. $^{13}\text{CO } J=1-0$ and CS $J=2-1$ are also detected toward each of the sources.

3.2.1. LkH α 198

Strong evidence for a blueshifted cavity centered on LkH α 198 at a position angle⁵ of $\sim 120^\circ$ is evident in the integrated channel maps of Figure 2. The same emission cavity is also obvious in the BIMA array data of Figure 3. This emission is likely associated with the cavity traced by near-IR I-band emission (Corcoran et al. 1995; Lagage et al. 1993; Leinert et al. 1991). The zeroth moment map of Figure 1 also highlights a weaker blueshifted feature to the southwest of the LkH α 198 sources (at a position angle

⁵ We define the position angle according to the component of the outflow which is most clearly defined.

TABLE 4
LkH α 198 AND SURROUNDING OBJECTS

Source	Other ID	R.A. (J2000.0)	Decl. (J2000.0)	Group ^a	Associated CO	Number of Associated Outflows	P.A. (deg east of north)
LkH α 198.....	V633 Cas	00 11 25.97	+58 49 29.1	II	Yes	2	$120^\circ, 70^\circ$
LkH α 198-IR.....	LkH α 198 B	00 11 26.22	+58 49 34.58	...	Yes	None	...
LkH α 198 mm	00 11 24.51	+58 49 42.81	...	Yes	1	350°
V376 Cas	00 11 26.21	+58 50 04.1	II	Yes	1	70°

NOTE.—Units of right ascension are hours, minutes, and seconds, and units of declination are degrees, arcminutes, and arcseconds.

^a Classification of Hillenbrand et al. (1992).

of $\sim 250^\circ$ east of north). This could be a portion of a second outflow centered on LkH α 198.

The appearance of a single extensive blue lobe to the northwest and driven by LkH α 198 is shown to be a result of resolution limitations in earlier data. Nakano et al. (1990) indicated that the velocity width of the blue lobe was significantly larger than the width of the red lobe they detected. Their single blue lobe is a combination of the blueshifted emission driven from V376 Cas and the young, embedded source LkH α 198 mm. However, the double-peaked, redshifted emission of Nakano et al. (1990) persists even in our higher spatial resolution data. The peak observed to the north of LkH α 198 may arise from redshifted emission from a LkH α 198–driven outflow in combination with emission from an outflow driven by LkH α 198 mm, while the redshifted emission to the south of LkH α 198 indeed arises from an outflow driven by that source. We suggest that at least one outflow is being driven from LkH α 198, based on the extended blueshifted cavity. LkH α 198-IR has been identified as the source associated with the cavity by Corcoran et al. (1995), but our $^{12}\text{CO } J = 1 - 0$ observations suggest that LkH α 198 is driving at least one outflow to the southeast.

Figure 1 compares the high-resolution $^{12}\text{CO } J = 1 - 0$ data with the polarized intensity at H band measured by Perrin et al. (2004a). The bipolar nebulosity centered on LkH α 198 in H-band emission has no counterpart in $^{12}\text{CO } J = 1 - 0$ from BIMA array data. In fact, the high-resolution components of the red- and blueshifted $^{12}\text{CO } J = 1 - 0$ emission are oriented primarily east and west of LkH α 198. The polarized emission should locate the circumstellar dust around the star; in this case, the north-south alignment could indicate the region of the star where the envelope has not yet been eliminated by the action of the outflow(s).

3.2.2. LkH α 198-IR

Based on Figure 1, there is little evidence for any significant outflow centered on LkH α 198-IR. Figure 4 shows that there is no high-velocity blue wing associated with the infrared source, and only a suggestion of slight redshifted emission. However, like LkH α 198, LkH α 198-IR shows strong self-absorption of the CO line, meaning that circumstellar gas is still associated with this object.

The cometary structure detected in intensity and polarization in the near-IR has no detected counterpart in $^{12}\text{CO } J = 1 - 0$ emission. It is difficult to reconcile the HH objects A and B from Corcoran et al. (1995) as originating from LkH α 198-IR without any hint of a $^{12}\text{CO } J = 1 - 0$ outflow in our data. In fact, there is a hint of a redshifted line wing in the $^{12}\text{CO } J = 1 - 0$ spectrum toward LkH α 198-IR (see Fig. 4). This could indicate a large-scale outflow contribution or ambient material contributions to the spectrum.

3.2.3. LkH α 198 mm

A roughly north-south outflow (with blueshifted emission at a position angle of $\sim 350^\circ$) from LkH α 198 mm is strongly suggested by Figures 1 and 2. The blueshifted component is particularly apparent in Figure 2 and appears quite localized to the source. This is also suggested by the BIMA array data alone in Figure 3, although we note that there is significant emission missing from this map. The red lobes of the outflows of LkH α 198 and LkH α 198 mm clearly overlap. It is certain that part of the $^{12}\text{CO } J = 1 - 0$ redshifted emission detected by Cantó et al. (1984) originates from this source and not LkH α 198.

Figure 4 shows the self-absorption present in all sources in the region, indicating substantial remaining circumstellar gas. Figure 4 also shows that the red lobe from LkH α 198 mm is much

stronger than the blue lobe. The fact that the outflow emission appears to lie so close to the driving source may indicate either that the outflow is almost entirely along the line of sight or that the driving source is very young. The absence of very high velocity line wings argues against a line-of-sight alignment. Superior resolution will be required to disentangle the outflow of LkH α 198 mm from the other outflows in the region and the ambient cloud. We note that the orientation of the outflow is completely consistent with a series of HH objects observed at position angles of 160° and 340° (Corcoran et al. 1995), which were attributed to LkH α 198, but are in fact more symmetric about LkH α 198 mm.

3.2.4. V376 Cas

Hillenbrand et al. (1992) categorize this source as a Group II HAeBe star, meaning that its spectral energy distribution is flat or rising toward longer wavelengths. We therefore expect that there is a substantial amount of cool material around the star that reprocesses more of the total radiation than could be explained by a flat disk. It is therefore not surprising that the $^{12}\text{CO } J = 1 - 0$ spectrum of this source shows evidence of self-absorption in Figure 4. Evidence for nebulosity has been previously noted to the west of V376 Cas by several authors (Leinert et al. 1991; Piirola et al. 1992; Smith et al. 2004). Leinert et al. (1991) used polarized imaging techniques to detect the elongation of this nebulosity (120°) and clearly identify V376 Cas as the illumination source of the nebula.

Figure 1 demonstrates the presence of extended, overlapping blue- and redshifted emission around this source at a position angle of $\sim 70^\circ$. The BIMA array data alone, shown in Figure 3, suggest that the strong blueshifted emission peak noted northwest of LkH α 198 in single-dish maps of the region may be dominated by emission from V376 Cas. This outflow orientation seems consistent with the nebulosity observed in the optical, given the difference scales to which those data and our molecular lines maps sample. The blue outflow is also coincident with the known HH objects to its east, designated HH162 (see Fig. 1 of Corcoran et al. 1995). The dominance of the blueshifted emission to the east and the lack of comparable redshifted emission to the west is entirely consistent with V376 Cas being located at the eastern edge of a small dark cloud core (see Fig. 1 in Smith et al. 2004).

4. LkH α 225S AND ENVIRONS

Another example of an HAeBe star in a group is LkH α 225. LkH α 225 comprises two sources separated by approximately $5''$ (Aspin et al. 1994): LkH α 225N and LkH α 225S (V* V1318 Cyg N and V* V1318 Cyg S) at a distance of 1 kpc (Cantó et al. [1984] after Herbig [1960]). At wavelengths longward of $5 \mu\text{m}$, LkH α 225 is the dominant source in the region ($L \sim 1600 L_\odot$, Thé et al. 1994). A third peak observed by Aspin et al. (1994) in the optical arises due to nebulosity between the two sources. This peak is coincident with the comma-shaped reflection nebula extending from LkH α 225N to LkH α 225S detected by Perrin et al. (2004b). Palla et al. (1995) detect two sources in the K band, with no evidence of the third source noted by Aspin et al. (1994); they also detect an H $_2$ O maser coincident with LkH α 225S lying at the center of a CO outflow. The detection of continuum peaks at the position of LkH α 225S at 1.3 mm (Henning et al. 1998) and in high-resolution imaging at 2.7 and 3.1 mm (Di Francesco et al. 1997; Looney et al. 2006) confirm that LkH α 225S is deeply embedded and likely the youngest star in the region. LkH α 225N is likely a pre-main-sequence star. Near-IR stellar spectra (Davies et al. 2001) show no absorption lines, only emission lines, making the identification of the spectral types of both stars difficult. Two other well-studied HAeBe stars are in the same region:

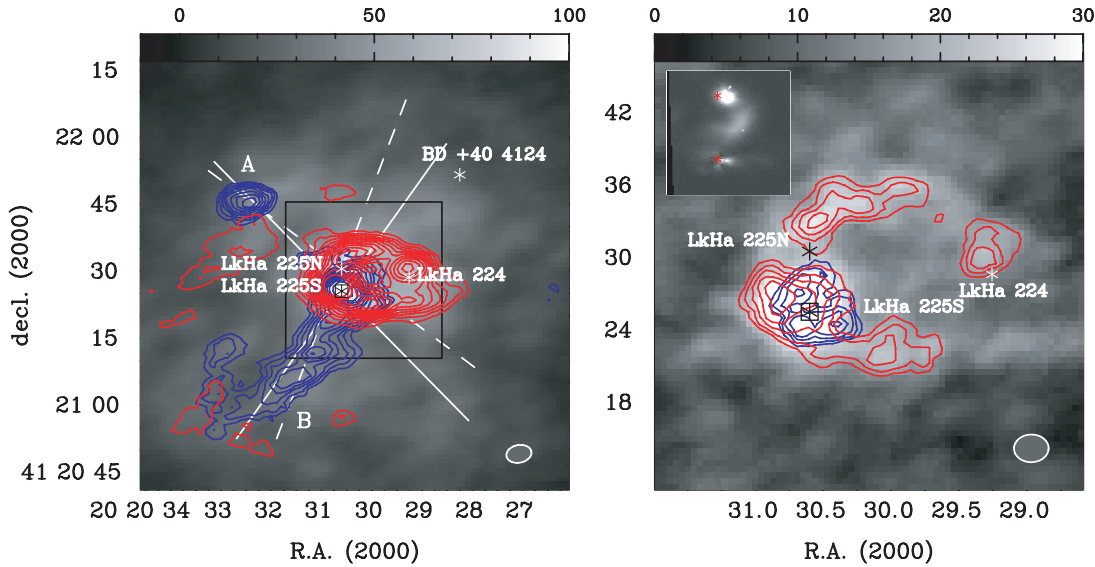


FIG. 5.—*Left*: Gray scale is the zeroth moment over the entire range of CO emission ($0\text{--}18\text{ km s}^{-1}$) of the combined FCRAO and BIMA array data toward the region centered on LkH α 225S (in units of $\text{Jy beam}^{-1}\text{ km s}^{-1}$). Optically visible HAeBe stars are marked by stars, while the embedded submillimeter source is indicated by a square. Contours trace blue emission from 0 to 4 km s^{-1} and red emission from 12 to 18 km s^{-1} . The blue contour levels range from 4.5 to $14.4\text{ Jy beam}^{-1}\text{ km s}^{-1}$ in steps of $0.9\text{ Jy beam}^{-1}\text{ km s}^{-1}$. The red contour levels range from 6.3 to 24.3 in steps of $1.8\text{ Jy beam}^{-1}\text{ km s}^{-1}$. The resolution is $5.7'' \times 4.0''$, or $5700\text{ AU} \times 4000\text{ AU}$ at 1 kpc . Two distinct blueshifted features, A and B, are observed. Position-velocity slices are taken through both features to align with the LkH α 225S (solid lines) and LkH α 225N (dashed lines) sources. The box shows the field of view of the uniformly weighted image at right. *Right*: Combined map generated with the uniformly weighted BIMA array data that yields a resolution of $2.87'' \times 2.29''$. The symbols and velocity ranges of the zeroth moment maps are the same as for the naturally weighted image. The blue contour levels range from 5 to $10\text{ Jy beam}^{-1}\text{ km s}^{-1}$ in steps of $1\text{ Jy beam}^{-1}\text{ km s}^{-1}$, and the red contour levels range from 10 to $20\text{ Jy beam}^{-1}\text{ km s}^{-1}$ in steps of $2\text{ Jy beam}^{-1}\text{ km s}^{-1}$. For comparison, the polarized intensity in H band as measured by Perrin et al. (2004b) is shown in the inset. The LkH α 225S and LkH α 225N sources are marked on this image.

BD +40 4124 (V1685 Cyg, MWC 340, IRAS 20187+4111) and LkH α 224 (V1686 Cyg), located approximately $50''$ to the northwest and $15''$ to the west, respectively, from the LkH α 225 sources. Looney et al. (2006) show that the LkH α 225 sources lie in the brightest molecular cloud core (as traced by BIMA array observations of CS $J = 2 - 1$) in an elongated molecular filament. CS $J = 2 - 1$ emission at $2.5''$ resolution is strongly peaked on LkH α 225S.

4.1. Observational Results

4.1.1. Moment and Channel Maps

Figure 5 shows the zeroth moment map summed from 0 to 15 km s^{-1} , and the distribution of emission blueward and redward of the source's LSR systemic velocity, 7.9 km s^{-1} (Palla et al. 1995). The $^{12}\text{CO } J = 1 - 0$ emission peaks around LkH α 225S. This concentration is unsurprising, since a submillimeter peak is also detected at its position, indicating that the associated source is still deeply embedded and very young. The uniformly weighted image shows clearly that the CO peaks do not coincide with the positions of the potential driving sources, indicating that the $^{12}\text{CO } J = 1 - 0$ emission associated with these sources is primarily in outflowing gas. Figure 6 shows channel maps of $^{12}\text{CO } J = 1 - 0$ emission. The $^{12}\text{CO } J = 1 - 0$ morphology is very complex, as evidenced by the variation of structure with velocity. The most intriguing structure is an apparent ring of emission, centered at $\alpha_{\text{J2000.0}} = 20^{\text{h}}20^{\text{m}}30.0^{\text{s}}$, $\delta_{\text{J2000.0}} = +41^{\circ}21'28.0''$, which persists over a large range of velocity ($10\text{--}18\text{ km s}^{-1}$). A SIMBAD⁶ search lists no objects at the center of the ring; the closest objects are the HAeBe stars in

the field. An H $_2$ O maser is reported at the position of LkH α 225S, identified as the driving source of the $^{12}\text{CO } J = 2 - 1$ outflow seen by Palla et al. (1995) at $15''$ resolution. The blueshifted emission detected by Palla et al. (1995) lies just to the east of the peak of the redshifted emission, implying that the outflow lies almost along the line of sight. Peaks on the ring are coincident with the positions of LkH α 224 and LkH α 225S, but LkH α 225N lies between $^{12}\text{CO } J = 1 - 0$ peaks. We surmise that the ring is the supposition of emission from several outflows, dominated by the pole-on outflow, which could have a substantial opening angle and could appear as a cylindrical cavity. No obvious counterpart to the ring is observed in blueshifted emission, but strong blueshifted emission is concentrated at the position of LkH α 225S.

To ascertain the physical origin of the “ring,” inspection of position-velocity ($P - V$) diagrams is critical. Figure 7 shows the difference between two $P - V$ slices, one taken centered on LkH α 225S and one taken at a position offset $24''$ to the south, with the same orientation. Taking the difference of these two $P - V$ diagrams crudely removes the large-scale emission from three separate molecular cloud components along the line of sight in Cygnus (at roughly 3 , 8 , and 13 km s^{-1}) and clearly reveals the presence of emission at the $0''$ offset across both red and blueshifted velocities (from 0 to 20 km s^{-1}) with respect to the source. The $P - V$ diagram produces this feature no matter what the orientation of the slice centered on LkH α 225S. We interpret this emission as arising from an outflow driven from LkH α 225S but observed almost pole-on. This is consistent with the $^{12}\text{CO } J = 2 - 1$ emission detected by Palla et al. (1995), in which they find strongly overlapping blue and red lobes in the single detected outflow. The blueshifted emission is offset slightly to the east compared to the red lobe, which is also consistent with the plane-of-sky emission shown in Figure 5, but is in the opposite sense to the outflow lobes observed by Palla et al. (1995).

⁶ Guest user, Canadian Astronomy Data Centre, which is operated by the Dominion Astrophysical Observatory for the National Research Council of Canada's Herzberg Institute of Astrophysics.

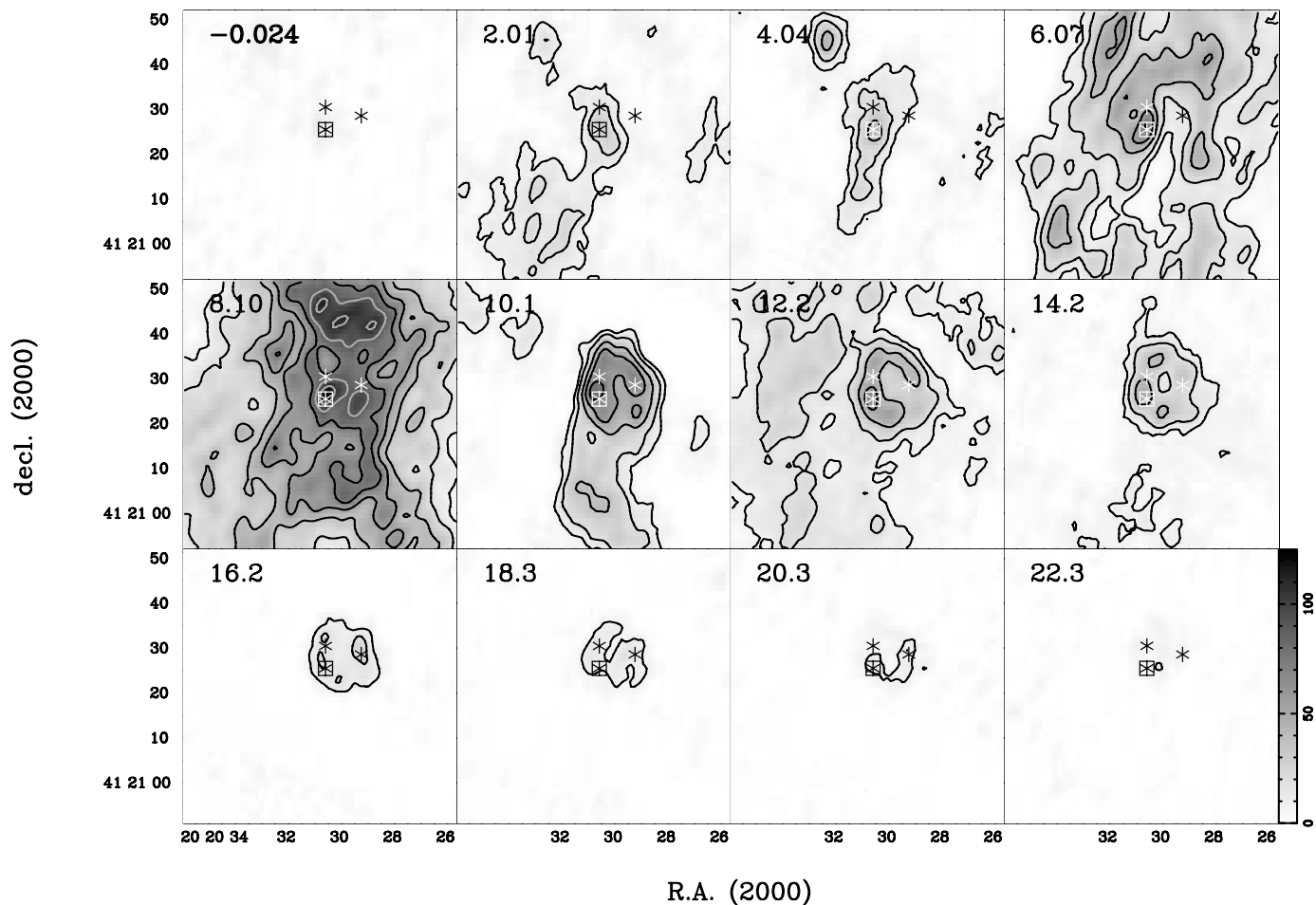


FIG. 6.—Binned velocity channels of $^{12}\text{CO } J = 1 - 0$ toward the LkH α 225S region are shown in gray scale and contours over 2.03 km s^{-1} bins. The mean velocity per channel is noted in km s^{-1} . The gray-scale range is common to all channels and is shown at right (Jy beam^{-1}). The contours are plotted at 20 and 40 to 360σ in steps of 40σ , where $\sigma = 0.45 \text{ Jy beam}^{-1}$ is the rms level in a single channel before binning. The sources are marked by asterisks and a square as in Fig. 5.

Figures 5 and 6 provide further clarification in identifying the driving sources of the outflows with components in the plane of the sky. In addition to the pole-on outflow, a second outflow appears well centered on LkH α 225, based on the blue lobe of emission detected southeast of the two sources at a position angle of $\sim 145^\circ$ (east of north). Another blue peak is detected to the northeast of the cluster of sources (at $\sim 45^\circ$), suggesting a third outflow is present in the system. There is no evidence of coherence in the blueshifted emission peaks to suggest they are part of a larger, blueshifted counterpart to the redshifted ring, i.e., part of the same outflow.

Figure 8 shows the $P - V$ diagrams across two position angles suggested by the orientation of the blueshifted emission detected in the zeroth moment and channel maps (labeled A and B in Fig. 5). Along these slices, there is evidence for redshifted components complementary to the blueshifted emission. The redshifted emission from these two potential outflows appears juxtaposed on the zeroth moment map of Figure 5, lying coincident with the redshifted gas from the pole-on outflow and creating a ring structure which persists over a range of velocities, although this emission appears significantly closer to the driving sources than the blue lobes.

4.1.2. Spectra

Using FCRAO, we have detected $^{12}\text{CO } J = 1 - 0$, $^{13}\text{CO } J = 1 - 0$, CS $J = 2 - 1$, and $\text{N}_2\text{H}^+ J = 1 - 0$ emission from

the LkH α 225S region. The $^{12}\text{CO } J = 1 - 0$, $^{13}\text{CO } J = 1 - 0$, and CS $J = 2 - 1$ spectra all indicate multiple emission peaks along the line of sight and are shown toward each of the four sources in Figure 9. We also show the combined $^{12}\text{CO } J = 1 - 0$ spectra at high spatial and spectral resolution. We show an $\text{N}_2\text{H}^+ J = 1 - 0$ spectrum toward LkH α 225S in Figure 10. Strong evidence for outflowing gas is detected toward LkH α 225S and LkH α 225N, but none is detected toward BD +40 4124 and only evidence for redshifted emission is seen at the position of LkH α 224. We interpret the high-velocity emission toward LkH α 224 as arising from the outflows generated by the LkH α 225 sources. Less ambient CO appears to be present in this region compared to the environment around LkH α 198, since no significant self-absorption is observed toward any of the sources in Figure 9. Interpretation of these spectra is further complicated by the presence of multiple clouds along the line of sight. Peaks are observed at five different velocities in the spectra ($1.6, 3.2, 7.9, 12.8,$ and 14.5 km s^{-1} as identified by eye in Fig. 9). The primary cloud, at 7.9 km s^{-1} , appears to contain all the H α eBe stars. A second cloud, at 12.8 km s^{-1} , appears to contain significant amounts of $^{12}\text{CO } J = 1 - 0$ and $^{13}\text{CO } J = 1 - 0$, but no CS $J = 2 - 1$ was detected at this velocity. The evidence for clouds at the remaining velocities is based on $^{12}\text{CO } J = 1 - 0$ only.

The resolution of FCRAO is such that we cannot be sure that all four sources are associated with dense gas. As the most embedded object, LkH α 225S is the most likely source to be

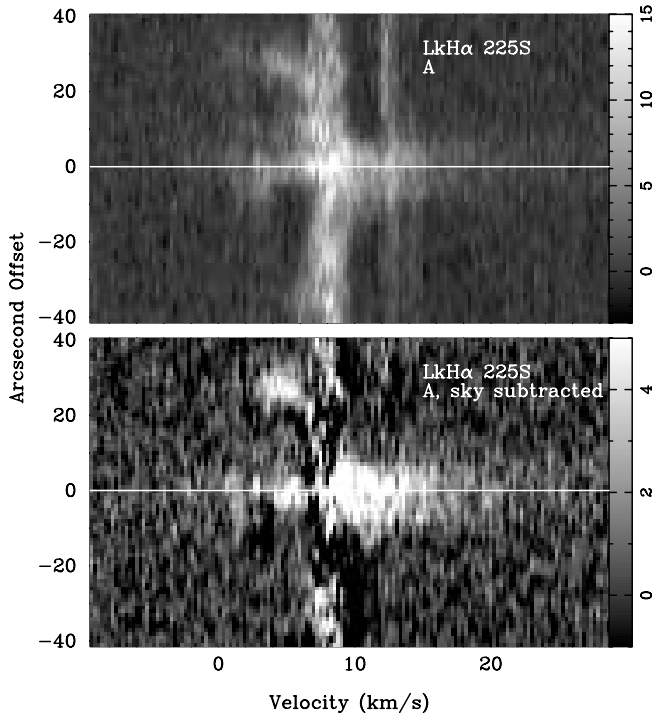


FIG. 7.— *Top*: Position velocity diagram taken centered on LkH α 225S, sliced through the blueshifted feature A of Fig. 5. The evidence for multiple clouds along the line of sight is indicated by the bands of emission at all angular positions. *Bottom*: Same position velocity slice, but with a second slice, positioned off the source 24'' to the southeast, subtracted from the on-source slice. The bulk of the cloud emission is removed, especially the fainter clouds. In this image, the most prominent feature is the emission extending from about 0 to 20 km s⁻¹ at zero angular offset. We interpret this as evidence for a pole-on outflow, most likely centered on LkH α 225S. Blueshifted emission is also detected to the northeast of LkH α 225S.

associated with dense gas. However, BD +40 4124, which is the furthest removed from LkH α 225S, lies only about 45'' distant. This is only one FCRAO beamwidth at the frequency of the ¹³CO $J = 1 - 0$ emission, and substantially less than a beamwidth in CS $J = 2 - 1$ and N₂H⁺ $J = 1 - 0$. Higher resolution observations can isolate the concentrations of these species and enable kinematic study of the associated cores.

4.1.3. 2.6 mm Continuum

No significant continuum was detected toward any of the sources in the field containing LkH α 225S. Our sensitivity is rather low, given the limited bandwidth available for continuum observations. We can put an upper limit of 51 mJy beam⁻¹ on the continuum flux on compact sources in the region. Despite the strong CO and N₂H⁺ $J = 1 - 0$ detections, we see no flux to attribute to either dust continuum or free-free emission. Di Francesco et al. (1997) detected 2.7 mm emission from LkH α 225S using the Plateau de Bure interferometer with a resolution of 6.8'' × 4.6''. They detected a peak flux density of 23 mJy beam⁻¹ and a total flux density of 24 ± 6.7 mJy. This flux would not have been detectable at a 2 σ level with the sensitivity ($\sigma = 17$ mJy beam⁻¹ rms) in our map.

4.2. Individual Sources

Table 5 summarizes our findings regarding ¹²CO $J = 1 - 0$ and outflows in this region. Self-absorption is not detected toward any sources in this field. However, we do detect tracers of dense gas, including ¹³CO $J = 1 - 0$, CS $J = 2 - 1$, and N₂H⁺

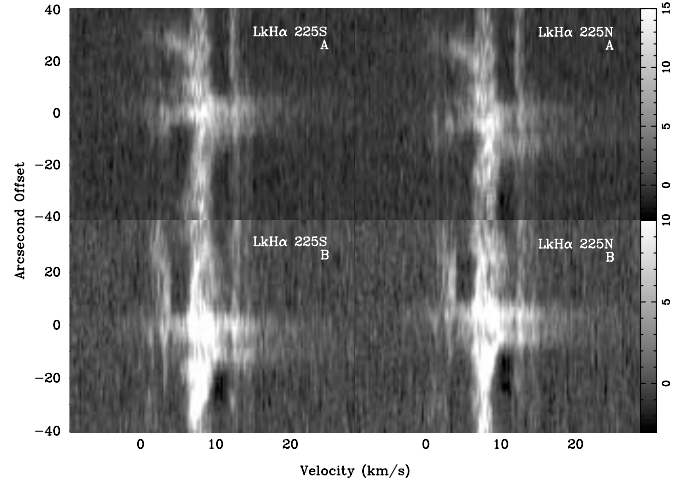


FIG. 8.— Position-velocity diagrams taken through the two blue features marked A and B in Fig. 5 are shown aligned through both the LkH α 225S and LkH α 225N sources. It is not possible to discriminate whether feature A arises from LkH α 225S or LkH α 225N. Feature B shows virtually the same profile through both sources. Since this feature is aligned with the offset between the sources, discrimination is naturally difficult. There is still some evidence for the pole-on outflow of LkH α 225S (see Fig. 7) in slices through LkH α 225N.

$J = 1 - 0$ in this cloud. We note also that our interpretations of outflows from LkH α 225S and LkH α 225N are still resolution limited. Therefore, we discuss these sources together below.

4.2.1. LkH α 225S and LkH α 225N

LkH α 225S is found to have evidence for up to three associated outflows. The most definitive connection is based on evidence for a nearly pole-on outflow clearly seen in the $P - V$ diagram of Figure 7. Evidence for two additional outflows is seen in Figure 5 in the form of two blueshifted emission features. The solid lines show the axes formed by the features, A and B, with LkH α 225S and both axes align with redshifted features seen on the other side of the potential driving source. However, LkH α 225S is separated from LkH α 225N by only 5'', which is comparable to the major axis of our synthesized beam (naturally weighted). This makes it difficult to associate decisively either of these two plane-of-sky outflows with LkH α 225S. Based on alignment, a strong case can be made that LkH α 225N is driving one or both of these outflows (see Fig. 5, *dashed lines*).

We assert that the apparent ring of Figure 5 has coherent structure, as it is dominated by the redshifted emission of the pole-on outflow with contributions from the other outflows originating from the LkH α 225 sources, one oriented at approximately 45°–55° east of north, the second at about 145°–160° east of north and the third almost pole-on toward us. No evidence of the ring morphology is observed in previous detections of high-velocity gas in the region (e.g., Palla et al. 1995) with resolution only a factor of 3 poorer than our data.

As we noted above, the interpretation of the ring as the redshifted counterparts to the more definitive blue lobes on the plane of the sky suggests that the red lobes have not expanded to the same spatial extent. The recent work of Looney et al. (2006) suggests a potential explanation. Their high-resolution BIMA array observations of CS $J = 2 - 1$ show that the CS $J = 2 - 1$ traces out a dense filament of emission to the northwest of the LkH α 225 sources. The presence of denser gas in this direction may be impeding the redshifted component of the outflow from extending into the cloud along these position angles.

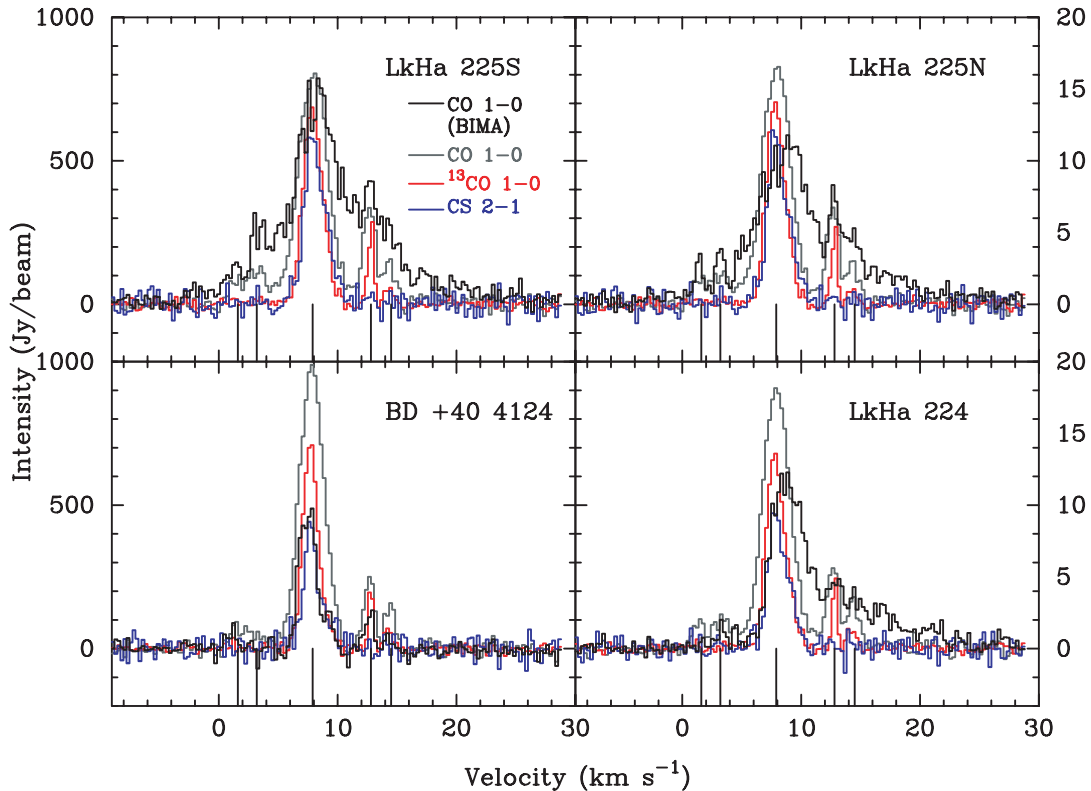


FIG. 9.— Spectra toward individual sources in the LkH α 225 region from FCRAO and FCRAO+BIMA array data. The spectral resolution is 0.254 km s^{-1} . Gray, red, and blue spectra represent $^{12}\text{CO } J=1-0$, $^{13}\text{CO } J=1-0$, and CS $J=2-1$ observations from FCRAO which were regridded to the spatial and spectral scales of the FCRAO+BIMA $^{12}\text{CO } J=1-0$ map. The intensity scale at the left is for the single-dish $^{12}\text{CO } J=1-0$ emission. The $^{13}\text{CO } J=1-0$ and CS $J=2-1$ emission have been multiplied by factors of 2 and 20. The black spectra are taken from the combined $^{12}\text{CO } J=1-0$ map. The intensity scale is shown at the right. Unlike the sources in the LkH α 198 region, those in Cygnus do not exhibit significant self-absorption. LkH α 225S and LkH α 225N show the most extensive line wings. BD +40 4124 does not show any evidence of outflow, while LkH α 224 shows no high-velocity blueshifted emission but extensive redshifted line wings which could be associated with another source in the field. The lines below the plots indicate $1.6, 3.2, 7.9, 12.8,$ and 14.5 km s^{-1} . These peaks each represent individual clouds along the line of sight.

4.2.2. BD +40 4124

BD +40 4124 is a Group I H AeBe star as classified by Hillenbrand et al. (1992). This means that there is no remaining circumstellar emission which cannot be accounted for by a disk. $^{12}\text{CO } J=1-0$, $^{13}\text{CO } J=1-0$, and CS $J=2-1$ are all detected toward BD +40 4124 based on the spectra of Figure 9. This emission is likely associated with the ambient molecular clouds along the line of sight to Cygnus. The lack of self absorption indicates that relatively little gas remains around this source, and there is no significant evidence of line wings in the spectra.

4.2.3. LkH α 224

LkH α 224 is also classified as a Group I H AeBe star by Hillenbrand et al. (1992). The spectrum of LkH α 224 is dominated by the multiple peaks associated with cloud emission along the line of sight. The combined $^{12}\text{CO } J=1-0$ spectrum does show evidence of a redshifted line wing, however. No outflow emission appears focussed on this source based on the channel maps of Figure 6, and no blueshifted emission is in the vicinity of this source in the zeroth moment map of Figure 5. Given its position relative to the blueshifted emission peaks, we surmise that the redshifted emission observed at the position of this source is part of one of the outflows originating from the LkH α 225 sources.

5. CONCLUSIONS

We find that the single bipolar outflow detected in the LkH α 198 region in single-dish maps is a combination of the redshifted

emission of the LkH α 198 and LkH α 198 mm outflows and the blueshifted components of the outflows from LkH α 198 mm and V376 Cas. In all, we find evidence for four outflows in the LkH α 198 region using high-resolution $^{12}\text{CO } J=1-0$ observations. Evidence for a cavity is observed in the LkH α 198 system along the same axis as the elliptical cavity detected in optical and IR emission. We see no evidence for circumstellar material based on $^{12}\text{CO } J=1-0$ emission associated with LkH α 198-IR, contrary

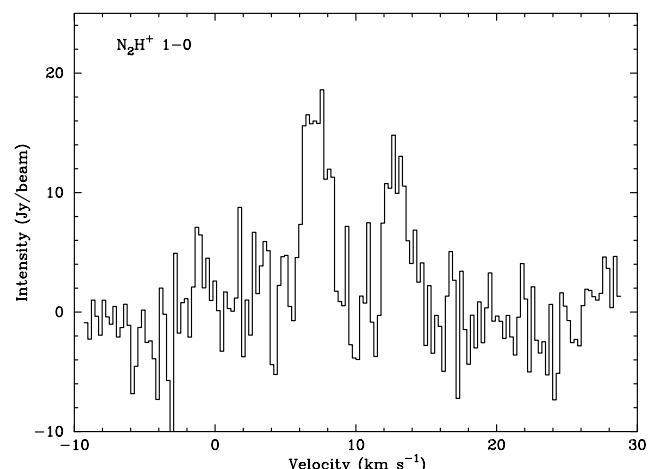


FIG. 10.— Spectrum of $\text{N}_2\text{H}^+ J=1-0$ emission toward LkH α 225S, indicating the presence of dense gas.

TABLE 5
LkH α 225S AND SURROUNDING OBJECTS

Source	Other ID	R.A. (J2000.0)	Decl. (J2000.0)	Group ^a	Associated CO	Number of Associated Outflows	P.A. (deg East of North)
LkH α 225S.....	V1318S Cyg	20 20 30.6	+41 21 25.5	...	Yes	1–3 ^b	l.o.s. ^c , 45°, 145°
LkH α 225N.....	V1318N Cyg	20 20 30.6	+41 21 30.5	...	Maybe	0–2 ^b	55°, 160°
BD +40 4124.....	V1685 Cyg	20 20 28.25	+41 21 51.6	I	Yes	None	...
LkH α 224.....	V1686 Cyg	20 20 29.26	+41 21 28.6	I	Yes	None	...

NOTE.—Units of right ascension are hours, minutes, and seconds, and units of declination are degrees, arcminutes, and arcseconds.

^a Classification of Hillenbrand et al. (1992).

^b The driving source of two outflows cannot be uniquely identified as LkH α 225S or LkH α 225N due to remaining resolution limitations.

^c Line of sight. The outflow is almost pole-on, with little component in the plane of the sky.

to the results from near-IR polarimetry which associate dust emission with that source (Perrin et al. 2004a) and observations of HH objects, which identified LkH α 198-IR as a driving source (Corcoran et al. 1995).

Our ability to discriminate between detected $^{12}\text{CO } J = 1 - 0$ outflows and to measure independent masses and momentum is limited by the single pointing of the BIMA array maps (Fig. 3 clearly shows that we have not mapped the outflows in their entirety) and spatial resolution. The outflow emission is still entangled and the cloud emission is also a contaminant. Ideally, mosaicked observations with various array configurations (including very close baselines) will be obtained to maximize the detection of the outflow emission, but minimize the detection of emission from the ambient cloud.

The $^{12}\text{CO } J = 1 - 0$ emission from LkH α 225S is equally complex. In all, we find evidence for up to three outflows in this region, all originating from the LkH α 225 sources. Large-scale cloud emission dominates the field, and multiple clouds along the line of sight contaminate the spectra. One is definitively associated with LkH α 225S and is almost entirely along the line of sight. The other outflows lie at angles of 35° and 135° east of north projected onto the plane of the sky. We suggest that the ring of redshifted emission is in fact a juxtaposition of the redshifted lobes of these two outflows, where their expansion has been hindered due to a dense molecular cloud lying to the northwest, with the cavity of the pole-on outflow (a coherent structure). As in the LkH α 198 region, higher resolution, mosaicked maps would help disentangle the outflows from the LkH α 225 sources.

Estimation of the mass in these outflows is not easy based on the data presented here because they can only be resolved within the BIMA array antenna field of view, whereas the outflows certainly extend to larger spatial scales. In several cases, emission from several outflows is clearly combined, further complicating the independent assessments of masses.

Finally, we find evidence of higher density gas in both regions, with $^{13}\text{CO } J = 1 - 0$ and CS $J = 2 - 1$ detected toward all eight sources and N $_2\text{H}^+ J = 1 - 0$ detected in the objects in Cygnus. Localizing the precise sources of this emission requires higher resolution observations, since the separation of sources is comparable to or smaller than the FCRAO beam.

The authors would like to thank Mark Heyer for advice and observing the FCRAO data for us. We thank J. Di Francesco for useful discussions and a careful reading of the manuscript. B. C. M.'s research was supported by an NSERC PDF and Berkeley NSF grant AST 02-28963. M. D. P. was supported by a NASA Michelson Fellowship. The BIMA array was operated with support from the National Science Foundation under grants AST-02-28963 to University of California, Berkeley, AST-02-28953 to University of Illinois, and AST-02-28974 to University of Maryland. FCRAO was supported by NSF grant AST 02-28993. This work has been supported by the National Science Foundation Science and Technology Center for Adaptive Optics, managed by the University of California at Santa Cruz under cooperative agreement AST-9876783.

REFERENCES

- Arce, H. G., & Sargent, A. I. 2006, *ApJ*, 646, 1070
Aspin, C., Sandell, G., & Weintraub, D. A. 1994, *A&A*, 282, L25
Bally, J., & Lada, C. J. 1983, *ApJ*, 265, 824
Cantó, Rodríguez, Calvet, & Levreault 1984, *ApJ*, 282, 631
Chavarría-K., C. 1985, *A&A*, 148, 317
Corcoran, D., Ray, T. P., & Bastien, P. 1995, *A&A*, 293, 550
Corcoran, M., & Ray, T. P. 1998, *A&A*, 336, 535
Davies, R. I., et al. 2001, *ApJ*, 552, 692
Di Francesco, J., Evans, N. J., II, Harvey, P. M., Mundy, L. G., Guilloteau, S., & Chandler, C. J. 1997, *ApJ*, 482, 433
Finkenzeller, U. 1985, *A&A*, 151, 340
Graham, J. R., Wright, G. S., & Longmore, A. J. 1987, *ApJ*, 313, 847
Hajjar, R., & Bastien, P. 2000, *ApJ*, 531, 494
Henning, Th., Burkert, A., Launhardt, P., Leinert, Ch., & Stecklum, B. 1998, *A&A*, 336, 565
Herbig, G. 1960, *ApJS*, 4, 337
Hernández, J., et al. 2004, *AJ*, 127, 1682
Hillenbrand, L. A., Strom, S. E., Vrba, F. J., & Keene, J. 1992, *ApJ*, 397, 613
Koresko, C. D., et al. 1997, *ApJ*, 485, 213
Lagage, P. O., Olofsson, G., Cabrit, S., Cesarsky, C. J., Nordh, L., & Rodriguez Espinosa, J. M. 1993, *ApJ*, 417, L79
Leinert, Ch., Haas, M., & Lenzen, R. 1991, *A&A*, 246, 180
Looney, L. W., Wang, S., Hamidouche, M., Safier, P. N., & Klein, R. 2006, *ApJ*, 642, 330
Matzner, C. D., & McKee, C. F. 2000, *ApJ*, 545, 364
McGroarty, F., & Ray, T. P. 2004, *A&A*, 420, 975
McGroarty, F., Ray, T. P., & Bally, J. 2004, *A&A*, 415, 189
McKee, C. F., & Ostriker, E. C. 2007, *ARA&A*, 45, 565
Mundt, R., & Ray, T. P. 1994, *ASP Conf. Ser.* 62, *The Nature and Evolutionary Status of Herbig Ae/Be Stars*, ed. P. S. The, M. R. Perez, & E. P. J. Van den Heuvel (San Francisco: ASP), 237
Nakano, M., Kogure, T., Yoshida, S., & Tatematsu, K. 1990, *PASJ*, 42, 567
Palla, F., Testi, L., Hunter, T. R., Taylor, G. B., Prusti, T., Felli, M., Natta, A., & Stanga, R. M. 1995, *A&A*, 293, 521
Perrin, M. D., Graham, J. R., Kalas, P., Lloyd, J. P., Max, C. E., Gavel, D. T., Pennington, D. M., & Gates, E. L. 2004a, *Science*, 303, 1345
———. 2004b, *SPIE*, 5490, 309
Pety, J., Gueth, F., Guilloteau, S., & Dutrey, A. 2006, *A&A*, 458, 841
Piirola, V., Scaltriti, F., & Coyne, G. V. 1992, *Nature*, 359, 399
Pyo, T., et al. 2003, *ApJ*, 590, 340
Racine, R. 1968, *AJ*, 73, 233
Sandell, G., & Weintraub, D. A. 1994, *A&A*, 292, L1
Sault, R. J., Teuben, P. J., & Wright, M. C. H. 1995, in *ASP Conf. Ser.* 77, *Astronomical Data Analysis Software and Systems IV*, ed. R. A. Shaw, H. E. Payne, & J. J. E. Hayes (San Francisco: ASP), 433

- Schmid-Burgk, J., Guesten, R., Mauersberger, R., Schulz, A., & Wilson, T. L. 1990, *ApJ*, 362, L25
- Smith, K. W., et al. 2004, *A&A*, 413, 217
- . 2005, *A&A*, 431, 307
- Stahler, S. W., & Palla, F. 2004, *The Formation of Stars* (Weinheim: Wiley-VCH), 452
- Stanimirovic, S., Staveley-Smith, L., Dickey, J. M., Sault, R. M., & Snowden, L. 1999, *MNRAS*, 302, 417
- Strom, K., et al. 1986, *ApJS*, 62, 39
- Testi, L., Palla, F., & Natta, A. 1998, *A&AS*, 133, 81
- Testi, L., Palla, F., Prusti, T., Natta, A., & Maltagliati, S. 1997, *A&A*, 320, 159
- Thé, P. S., de Winter, D., & Pérez, M. R. 1994, *A&AS*, 104, 315
- Waters, L. B. F. M., & Waelkens, C. 1998, *ARA&A*, 36, 233
- Welch, J. W., et al. 1996, *PASP*, 108, 93
- Zhang, Q., et al. 2007, *ApJ*, 658, 1152